Fermi National Accelerator Laboratory

FERMILAB-Conf-96/011

Simulation of Backgrounds in Detectors and Energy Deposition in Superconducting Magnets at $\mu^+\mu^-$ Colliders

N.V. Mokhov and S.I. Striganov

Fermi National Accelerator Laboratory
P.O. Box 500, Batavia, Illinois 60510

Institute for High Energy Physics
Protvino, 142284, Russia

January 1996

Proceedings of the *9th Advanced ICFA Beam Dynamics Workshop: Beam Dynamics and Technology Issues for* $\mu^+\mu^- Colliders, Montauk, New York, October 15-20, 1995$

Operated by Universities Research Association Inc. under Contract No. DE-AC02-76CHO3000 with the United States Department of Energy

Disclaimer

Simulation of Backgrounds in Detectors and Energy Deposition in Superconducting Magnets at $\mu^+\mu^-$ Colliders*

N. V. Mokhov and S. I. Striganov+

Fermi National Accelerator Laboratory

P.O. Box 500, Batavia, Illinois 60510

+ *Institute for High Energy Physics, Protvino, 142284, Russia*

January 16, 1996

Abstract

A calculational approach is described to study beam induced radiation effects in detector and storage ring components at high-energy high-luminosity $\mu^+\mu^-$ colliders. The details of the corresponding physics process simulations used in the MARS code are given. Contributions of electromagnetic showers, synchrotron radiation, hadrons and daughter muons to the background rates in a generic detector for a 2×2 TeV $\mu^+\mu^-$ collider are investigated. Four configurations of the inner triplet and a detector are examined for two sources: muon decays and beam halo interactions in the lattice elements. The beam induced power density in superconducting magnets is calculated and ways to reduce it are proposed.

* In *Proceedings of the 9th Advanced ICFA Beam Dynamics Workshop: Beam Dynamics and Technology Issues for $\mu^+\mu^-$ Colliders*, Montauk, NY, October 15-20, 1995

INTRODUCTION

Recent studies on a high-energy high-luminosity $\mu^+\mu^-$ collider [1, 2] have shown the high physics potential and a feasibility of such a project. A candidate design for 2×2 TeV machine, based on the existing and near-term technology, with a luminosity as high as 10^{35} cm^{-2} s^{-1} is described in [3]. The two most serious beam-related problems envisioned on the way to the practical realization of a storage ring are enormous particle background levels in a detector and a high power density in the superconducting magnets [4, 5, 6] due to unavoidable muon decays and beam halo interactions. With 2×10^{12} muons in a bunch at 2 TeV one has 2×10^5 decays per meter in a single pass through an interaction region (IR), or 6×10^9 decays per meter per second.

Decay electrons with an energy of about 700 GeV and the enormous number of synchrotron photons emitted by these electrons in a strong magnetic field induce electromagnetic showers in the collider and detector components resulting in high radiation and background rates. Another contribution comes from beam halo interactions at the limiting apertures.

A first-pass study [4] showed that the electromagnetic component of the backgrounds from $\mu \to e\nu\tilde{\nu}$ decays has the potential of killing the concept of the muon collider without significant suppression via various shielding and collimators in the detector vicinity. Beam induced energy deposition in the superconducting (SC) magnets may result in magnet quench and in high heat load to the cryogenic system which also requires special protection measures and a serious design effort [5].

In this paper a calculational stream and the corresponding physics algorithms used to study beam related effects in a muon collider lattice (Fig. 1) and a generic detector (Fig. 2) are described. Electron, positron and photon fluxes as well as photo-hadron and photo-muon contributions are examined for four inner triplet and detector configurations. Detailed calculations and analysis are performed to study the physics phenomena resulting in particle fluxes in detectors and energy deposition in magnets. Results on beam induced heat load in the muon collider SC magnets are presented. Efficacy of possible measures to reduce background and heat load levels are analyzed quantitatively.

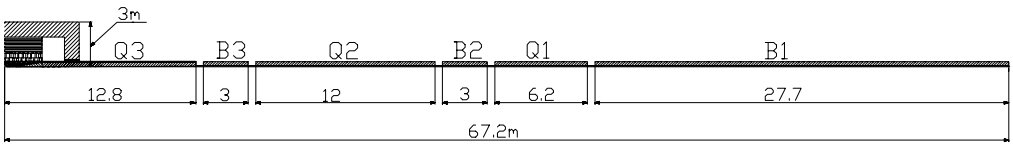

FIGURE 1. Schematic of muon collider inner triplet and detector [4] (Configuration 1) . Dimensions are in meters.

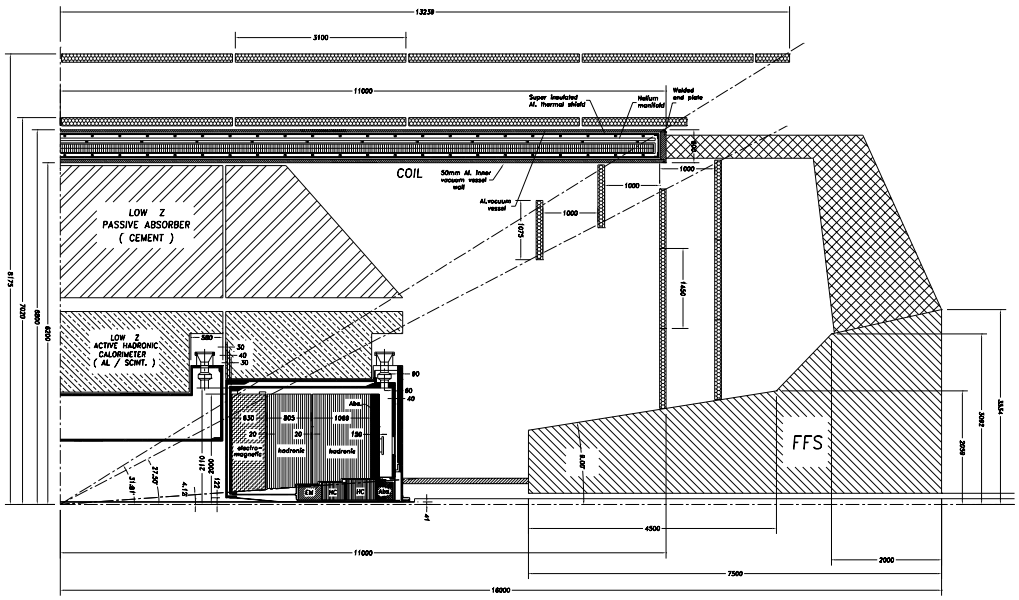

FIGURE 2. Schematic view of realistic detector [7] (Configurations 3 and 4).

CALCULATIONAL STREAM

All the calculations are done with the MARS code [8]. Recent code modifications relevant to the studied problem include: a better description of muon cross-sections, of muon decay and of the algorithm for electromagnetic fluctuations [9]; an improved particle transport algorithm in a magnetic field; synchrotron radiation generation; generation of hadrons in photo-nuclear interactions and muons in the course of electromagnetic shower development; modified geometry description; extended histogramming and graphical possibilities.

Simulations with the MARS code are done for the realistic lattice extended up to 300 meters from the interaction point (IP) including the detailed dipole and quadrupole geometry and magnetic field maps [4, 5]. All the particle interaction processes in the lattice, the 1.45 m radius tunnel surrounded by rock, the experimental hall 26 m long, 10 m radius) and the detector are taken into account.

A single MARS run includes:

- Forced $\mu \to e \nu \tilde{\nu}$ decays in the beam pipe (beam muon decay studies) or beam tail interactions with the limiting aperture beam pipe (beam halo studies).

- Tracking of created electrons in the beam pipe under the influence of the magnetic field with emission of synchrotron photons along the track.

- Simulation of electromagnetic showers in the collider and detector components induced by electrons and synchrotron photons hitting the beam pipe,

with the appropriate hadron and prompt muon production (Bethe–Heitler pairs and direct positron annihilation).

- Simulation of muon interactions (bremsstrahlung, direct e^+e^- pair production, ionization, deep inelastic nuclear interactions and decays) along the tracks in the lattice, detector, tunnel and experimental hall components as well as with tunnel and hall air and the surrounding rock.

- Simulation of electromagnetic showers created in the above muon interaction vertices.

- Simulation of hadronic cascades generated in muon and photon interactions, with daughter electromagnetic showers, with muon production (π and K decays, prompt muons in hadronic and electromagnetic interactions), and with low–energy neutron transport.

- Histogramming and analysis of particle energy spectra, fluences and energy deposition in various detector and collider regions.

Energy thresholds are 1 MeV for muons and charged hadrons, 0.3 MeV for electrons and photons, and 0.00215 eV for neutrons. In this study we assume that a bunch of 2×10^{12} muons of 2 TeV energy enters the inner triplet moving toward the IP, creating showers responsible for backgrounds along its path. Only a single bunch is simulated to study the directionality which is masked in the case of two colliding beams. When studying the integrated effect, we assume 1000 turns as a beam lifetime.

The physics model and corresponding calculational algorithms for particle interactions and transport and for geometry definition are described in detail elsewhere (see [8, 10] and bibliography there). The next section highlights muon interaction specifics.

SIMULATION OF MUON INTERACTIONS

Muons decay in flight producing energetic electrons. In the MARS code the synchrotron radiation spectrum for electrons in a magnetic field is taken from References [11] and [12] with the number of photons sampled from a Poisson distribution. These electrons and photons initiate electromagnetic showers in accelerator and detector components causing the severe background and radiation problems. Muons generated in electromagnetic showers and beam halo muons do penetrate through the bulk of material and contribute to the rates cumulatively from the extended regions of the collider. When high energy muons pass through matter all their interaction processes result in energy loss, production of photons, electrons and hadrons which accompany the muon track and are taken into account in the MARS code. For a 1 TeV muon in iron the mean energy loss rates due to ionization, bremsstrahlung,

direct e^+e^- pair production and photo-nuclear interaction are 2.32, 2.92, 4.16 and 0.39 MeV/g/cm^2, respectively.

$\mu \longrightarrow e\nu\tilde{\nu}$ Decays

Vector momentum of the emitted electron is sampled according to the differential decay probability of the *Vector–Axial* model of four-fermion interactions [12]. All measurements in direct muon decay $\mu \rightarrow e\nu\tilde{\nu}$ are successfully described by this model.

Ionization Energy Loss

Collisions of charged particles and atoms with energy transfer ε greater than some cutoff ε_c are considered in MARS as discrete events involving production of δ-electrons, e^+e^--pair, bremsstrahlung. Energy losses with $\varepsilon < \varepsilon_c$ (so called restricted losses) are taken into account as continuous.

Several methods have been offered to simulate fluctuations of restricted losses for ionization [9, 13, 14]. All of them use Vavilov's function [15] for this purpose with redefined parameters

$$\xi = Bs$$

$$B = 0.1536Z/A/\beta^2$$

$$\kappa_n = \xi/\varepsilon_G$$

$$\beta_n^2 = \beta^2\varepsilon_G/\varepsilon_{max},$$

where Z and A are the absorber atomic and mass numbers, β is the particle velocity, s is the path length in g/cm^2, and ε_{max} is the maximum energy transferred in a single collision. With $\varepsilon_G < \varepsilon_c$ Vavilov's function becomes Gaussian asymptotically for $\kappa > 10$ [15]. Therefore for

$$\kappa_n > 10 \tag{1}$$

the restricted loss distribution becomes Gaussian with the mean

$$\bar{\Delta}_r = \alpha(\varepsilon < \varepsilon_G) \cdot s$$

and the variance

$$\sigma_r^2 = \frac{\xi^2}{\kappa_n}(1 - \frac{\beta_n^2}{2}),$$

where $\alpha(\varepsilon < \varepsilon_c)$ is the mean restricted energy loss per unit length.

For the simulation of δ-electrons with energy greater than ε_δ at any step, ε_G is calculated using (1) and the restricted energy loss with $\varepsilon_c = min(\varepsilon_G, \varepsilon_\delta)$ is sampled.

Then, the number of δ-electrons is simulated using a Poisson distribution. The coordinates of δ-electron generation are obtained with the following recursive procedure

$$x_n = x_{n-1} + (1 - (1 - g_n)^{1/(k-n+1)})(s - x_{n-1})$$

and

$$x_0 = 0,$$

where k is a number of δ-electrons, $x_n$are the coordinates of production points along the step ($1 \leq n \leq k$) and g_n are random numbers uniformly distributed on (0,1). The electron energies are sampled from the well-known Bhabha formulae. Total energy loss of a particle is the sum of the δ-electron energies and of the restricted energy loss.

Radiative Energy Loss

For high energy muons (E $\geq$ a few hundred GeV), the radiative mechanisms, bremsstrahlung and direct e^+e^- pair production, will dominate over the ionization losses. An exact but complicated expression has been given by Kel'ner [16]. One performs a two-fold numerical integration to calculate the differential cross section using this approach. Therefore approximations of Kel'ner's results are usually used in Monte Carlo calculations. However, the accuracy of these approximations is not very high. Even the mean energy loss differs by more than 10% from Kel'ner's calculations.

At the same time, the numerical integration shows that only the first two moments of the pair production cross section give a sizable contribution to the moments of the total electromagnetic cross section. Relative contributions for higher moments do not exceed a few percent. Therefore, in MARS a simple function [17] is used to approximate the pair production cross section:

$$\frac{d\sigma_p}{d\nu} = b_p \frac{a(1+a)}{\nu(\nu+a)^2}, \tag{2}$$

$$b_p = (\frac{1}{E}\frac{dE}{dx})_p,$$

where $(dE/dx)_p$ is the mean energy loss per unit length. The following expression approximates b_p with a few percent accuracy:

$$b_p = 1.689 \cdot 10^{-5} \frac{m_e}{M} \frac{Z(Z+1)}{A} \left[b_1 ln\left(\frac{b_3 Z^{-1/3}}{1 + 4b_3 Z^{-1/3} M/E} \right) - b_2 \right], \ [\frac{cm^2}{g}]. \tag{3}$$

Here M and m_e are the incident particle and electron masses, respectively.The parameter a is determined from the second moment of the cross section

$$a = \begin{cases} a_1 \cdot 10^{-3} m_\mu / M \ , & E \leq a_3; \\ (a_1 + a_2 ln(E/a_3)) \cdot 10^{-3} m_\mu / M, & E > a_3, \end{cases}$$

Table 1: Parameters of the approximation for pair production cross section.

	Muon $E > 20$ GeV	Pion $E > 20$ GeV	Kaon $E > 50$ GeV	Proton $E > 90$ GeV
a_1	5.2	5.5	5.45	5.4
a_2	.13	.18	.35	.43
a_3 (GeV)	200	200	100	100
b_1	.787	.791	.819	.833
b_2	1.1	1.09	1.14	1.17
b_3	2986	3017	2773	2532

where m_μ is the muon mass. The parameters a_i, b_i for some charged particles are given in Table 1. To sample the angles of e^+, e^- and muons after the interaction, the method proposed in [18] is used.

There is a number of different approaches for the calculation of the muon bremsstrahlung cross section (see [19] for recent discussion). These methods differ mainly in the treatment of screening corrections. In MARS a general expression proposed in [19] is used, which allows arbitrary nuclear and atomic formfactors to be applied.

For a small energy transfer $\varepsilon < \varepsilon_\gamma = 10^{-3}E$ at a muon energy $E > 10$ GeV, the bremsstrahlung differential cross section reaches the complete screening limit

$$\Sigma_\gamma(E,\varepsilon) = \frac{d_\gamma}{\varepsilon},$$

where $d_\gamma = 4b_\gamma/3$ and

$$b_\gamma = (\frac{1}{E}\,\frac{dE}{dx})_\gamma.$$

With this, the restricted energy loss distribution can be approximated by

$$f_c^\gamma(\Delta_c, E, s) \simeq \frac{d_\gamma s}{\varepsilon_c^{d_\gamma s}} \frac{1}{\Delta_c^{1-d_\gamma s}}. \tag{4}$$

The continuous energy loss Δ_c at a step s is sampled from (4) providing $\Delta_c < \varepsilon_c < \varepsilon_\gamma$. The production of bremsstrahlung photons with energies greater then ε_c is considered as a discrete process. Fig. 3 shows muon differential cross-sections for bremsstrahlung calculated by four different programs.

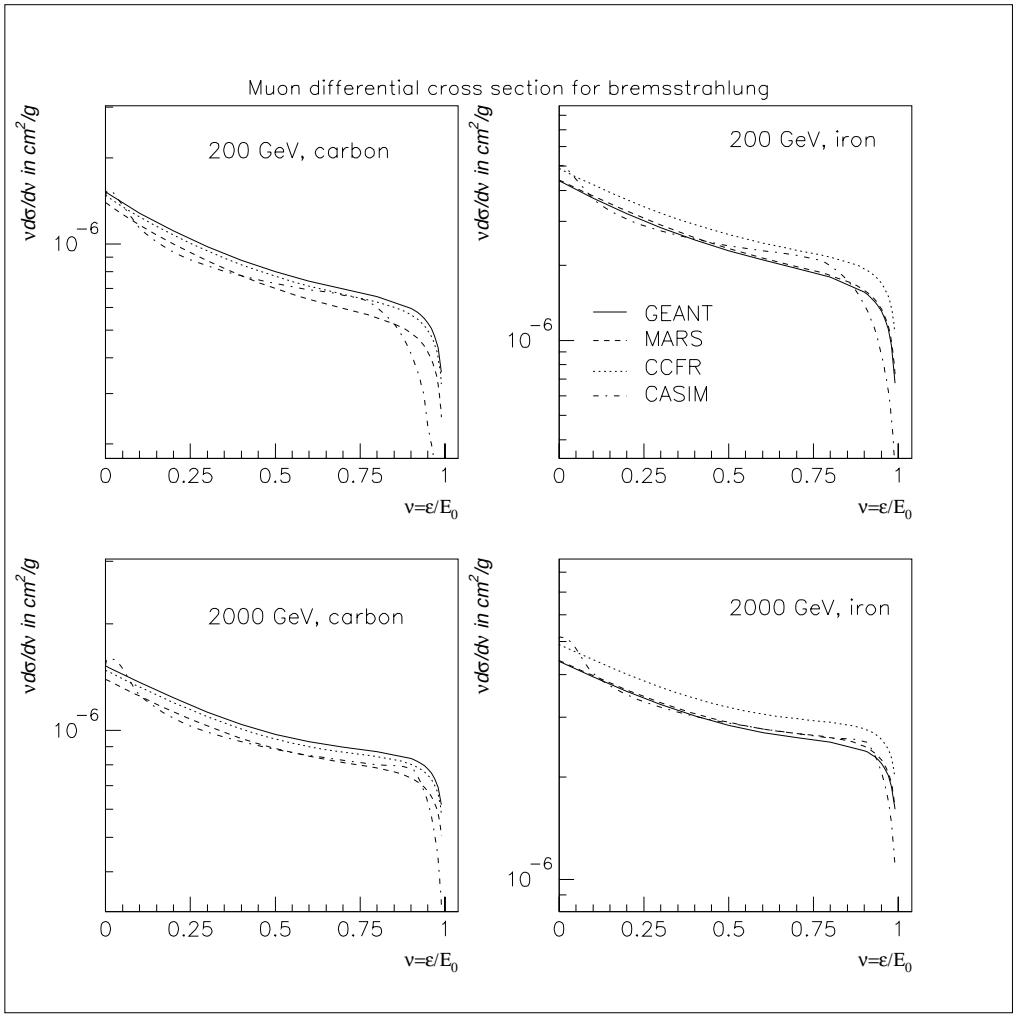

FIGURE 3. Muon differential cross-section for bremsstrahlung in carbon and iron at E_0 = 200 GeV and 2000 GeV *vs* energy transferred to photons, as used in GEANT [20], MARS [19], in CCFR collaboration [22], and in CASIM [18] (approximation of Tsai formula).

Deep Inelastic Interactions

Different models of deep inelastic muon-nucleus scattering are consistent at the 30% accuracy level. At the same time, the relative mean energy loss for this process is $\leq 10\%$ of the total, even at very high energies. The corresponding mean free path exceeds ~ 100 meters of iron for muons in the TeV energy region. So, high precision in a deep inelastic interaction description is not of primary importance. We choose the formula evaluated in [21], which is in good agreement with recent experimental data [22].

$\gamma A \rightarrow hX$ Reactions

Hadroproduction in photon-nucleus interactions at $E_\gamma \geq 0.14$ GeV is simulated in an approximate way. The photon is replaced with a real pion of random charge with the same kinetic energy. The total cross section is calculated as

$$\sigma_{\gamma A} = R_A \cdot (Z\sigma_{\gamma p} + (A - Z)\sigma_{\gamma n}). \quad (5)$$

For the total γp cross section experimental data are used from [23] at momentum below 4.215 GeV/c and the fit from Review of Particle Properties [24] at higher energies. For the total γn cross section experimental data from [25] at momentum below 4 GeV/c and a fit from [26] at higher energies are used.

The A-dependence of the cross section R_A in (5) is extracted from experimental data: recent data [27] at E $\leq$ 1.15 GeV, and the approximation $R_A = 1.047A^{-0.085}$ at higher energies. The quality of this description in comparison with available experimental data is shown in Fig. 4.

Photoneutron production in the giant resonant energy region $6 \leq E_\gamma \leq 60$ MeV is described according to the algorithm [28, 29] extended for light nuclei $4 \leq A \leq 56$ on the basis of the latest data. An interpolation is used between 60 and 140 MeV.

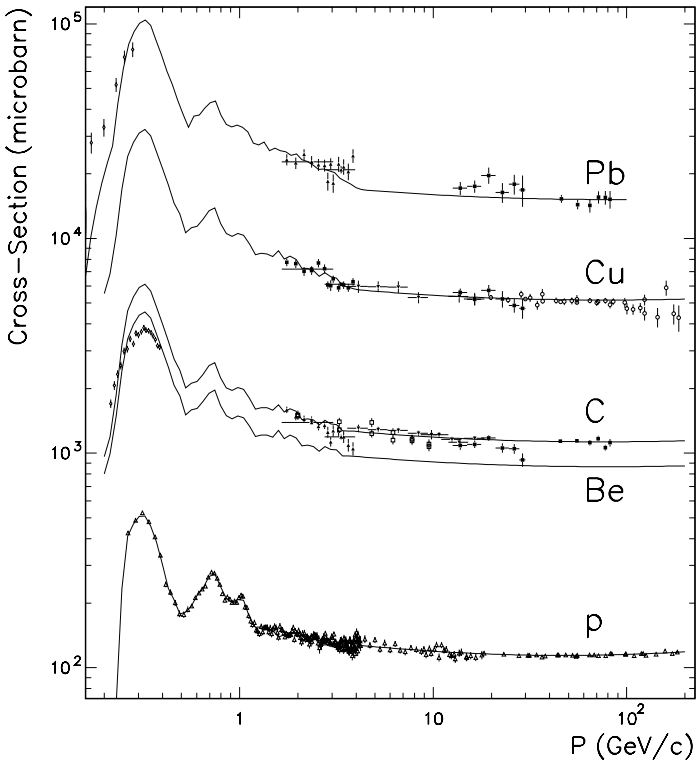

FIGURE 4. Calculated photon-nucleus cross-section in comparison with experimental data *vs* photon momentum for lead, copper, carbon, beryllium and hydrogen.

DAUGHTER MUON PRODUCTION

Processes responsible for muon generation at the above stages in the induced hadronic and electromagnetic cascades are included in the MARS code.

Hadronic Interactions

Simulation algorithms for $\pi^{\pm} \to \mu^{\pm} \nu(\tilde{\nu})$ and $K^{\pm} \to \mu^{\pm} \nu(\tilde{\nu})$ decays and for prompt muon production (single muons in charmed meson decays, $\mu^+\mu^-$ pairs in vector muon decays, and the dimuon continuum) with forced generation of weighted muons are described in [8, 10].

Electromagnetic Showers

Prompt muons produced by electrons and photons are handled by the current MARS version [8, 30]. Bethe-Heitler pairs $\gamma Z \to Z \mu^+ \mu^-$ are produced at $E_\gamma \geq 0.25$ GeV at a rate of $(m_e/m_\mu)^2$ times that for e^+e^- with the appropriate statistical weights and a complete simulation of the electromagnetic showers, similar to the MUSIM code [31]. It was shown [30] that this approach gives results in remarkable agreement with those based on the numerical integration in the Tsai formalism [32].

At $E \geq 45$ GeV direct positron annihilation $e^+ e^- \to \mu^+ \mu^-$ is simulated according to [12] with the cross section $86.8/s$ nb, where s is in GeV^2, and the $(1 + cos^2\theta)$ angular distribution.

LATTICE AND DETECTOR CONFIGURATIONS

Beam muon decays and beam halo interactions in the inner triplet and adjacent regions have been studied in four lattice-detector configurations for a 6 km circumference 2×2 TeV storage ring.

Configuration 1

The first configuration is examined for a distance L $\leq$ 70 m from the IP for the inner triplet with β^*=3 mm and β_{peak}=400 km [4]. Superconducting dipole magnets B1, B2 and B3 have a central field 8 T (Fig. 1). Combined function superconducting quadrupoles Q1 and Q2 are have a 2 T dipole component and a gradient of 50 T/m. All of the SC components have an 8 cm radius aperture. The Q3 quadrupole is resistive with a 0.5 T dipole field, except the first 1.3 m near the IP where the dipole component is equal to zero. Its aperture is reduced toward the IP from R=4.5 cm at L=12.8 m to R=0.45 cm at L=1.2 m, with the gradient increasing from 33.3 T/m to

333.3 T/m, appropriately. Geometries and materials of beam pipes, collars, yokes and cryostats for the SC dipoles and quadrupoles as well as the 2-D POISSON calculated magnetic fields in these components are embedded in the calculational package. A copper bucking coil is placed on the outside of the Q3 to neutralize the effect of the solenoidal field in the quadrupole.

A rather simple model detector is used (Fig. 1) [4]: a two-region silicon tracker with volume averaged density $\rho = 0.15$ g/cm^3, a central calorimeter (CH, $\rho = 1.03$ g/cm^3) and a solenoid magnet with 2 Tesla magnetic field.

Configuration 2

This configuration is based on the first complete lattice of the 2×2 TeV $\mu^+\mu^-$ storage ring. It was found [5] that a suppression of synchrotron radiation generation is possible by using single function quadrupoles in the triplet and by keeping the high field dipoles as far from the IP as possible. In a prototype lattice [5] with β^*=3 mm, β_{peak}=200 km, the low-β quadrupoles have a gradient of 262 T/m and the nearest 8 T SC dipole starts at L=130 m from the IP. The detector configuration is as in the first case. Calculations have been carried out for the region L $\leq$ 300 m from the IP with and without some collimators there.

Configuration 3

The previous lattice with a much more realistic detector (Fig. 2) is used in this configuration. Detector design is based on GEM and ATLAS detector ideas adopted to the muon collider [7]. The detector consists of an inner tracker, Pb-LAr/Cu-LAr electromagnetic calorimeter followed by Al-Sci hadronic calorimeter, low-Z passive absorber and a superconducting solenoid surrounded with muon chambers. In the forward direction it has an endcap calorimeter and forward muon spectrometer. Studies are performed for L $\leq$ 300 m from the IP.

Configuration 4

A more practical lattice of lower luminosity designed by K. Y. Ng is adopted. The final focus is a doublet with β^*=3 cm, β_{peak}=31.4 km. The first 6.3 m long low-β quadrupole, still inside the detector, starts at 6.5 m, which is much father compared to the previous cases. A second 6 m quadrupole, just 0.13 m away, is followed by about 20 m of drift. Both quadrupoles have a tapered SC coil aperture of 2.5 cm radius at L=6.5 m and 6.1 cm radius at L=18.93 m. The pole tip field is 9.5 T. The coil aperture radius of the rest of the machine is assumed to be 7 cm. A tungsten liner (flared in the doublet) occupies the allowable space in the aperture. The realistic detector description of Fig. 2 is used. To study in detail the importance of various parts of the final focus, the contribution to the backgrounds is explored for a short region L $\leq$ 30 m.

BACKGROUNDS IN DETECTORS

Muon Decays

Typical particle spectra integrated over the whole system are shown in Fig. 5. The results are normalized to a single pass, so the relative importance of different components is clearly seen. The peak sitting around 700 GeV in the e^+e^- spectrum represents the $\mu \to e\,\nu\tilde{\nu}$ decay spectrum with a tail at lower energies enriched by electrons and positrons of electromagnetic showers induced in the beam pipe and superconducting coils. Photons emitted due to synchrotron radiation along e^+e^- tracks in a strong magnetic field have a peak around 1 GeV. Neutron spectra (not shown) have pronounced peaks at ≈80 MeV and ≈0.8 MeV, and a 1/E slope down to the thermal peak. Neutrons, along with photons, dominate in total flux, especially at large radii.

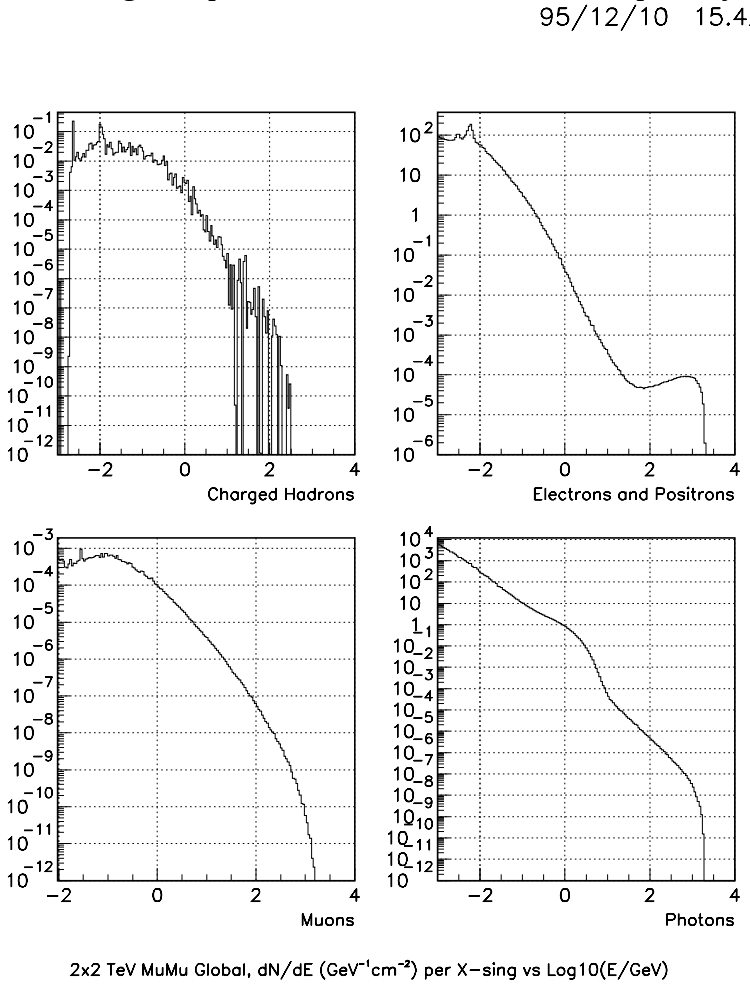

FIGURE 5. Particle spectra averaged over the interaction region and detector with 2 TeV muon decays as a source (Configuration 4).

Due to the very high energy of electrons and photons in the large aperture, the whole triplet is a source of backgrounds in the detector. As calculated in [4], e^+e^- and photon fluxes and energy deposition density in detector components are well beyond current technological capabilities if one applies no measures to bring these levels down. The most effective collimation includes a limiting aperture about one meter from the IP, with an interior conical surface which opens outward as it approaches the IP (Fig. 6). These collimators have the aspect of two nozzles spraying electromagnetic fire at each other, with the charged component of the showers being confined radially by the solenoidal magnetic field and the photons from one nozzle being trapped (to whatever degree possible) by the conical opening in the opposing nozzle.

A few collimator configurations occupying the cone $\theta < 150$ mrad in the $15 < L < 120$ cm region on the either side of the IP are studied (Fig. 6). Collimators made of tungsten as well as of a combination of various materials (aluminum, copper and tungsten) with different hole shapes have been considered. It turns out that for the main source of the backgrounds, direct muon decays, the best choice is a tungsten nozzle with an aperture radius R=0.45 cm at L=120 cm and R=1 cm at L=15 cm. The background reduction is amazing. The e^+e^- fluence calculated in [4] for Configuration 1 is given in Table 2. There is a significant difference in the background levels in the left (outward) and in the right (inward) parts of the tracker and calorimeter.

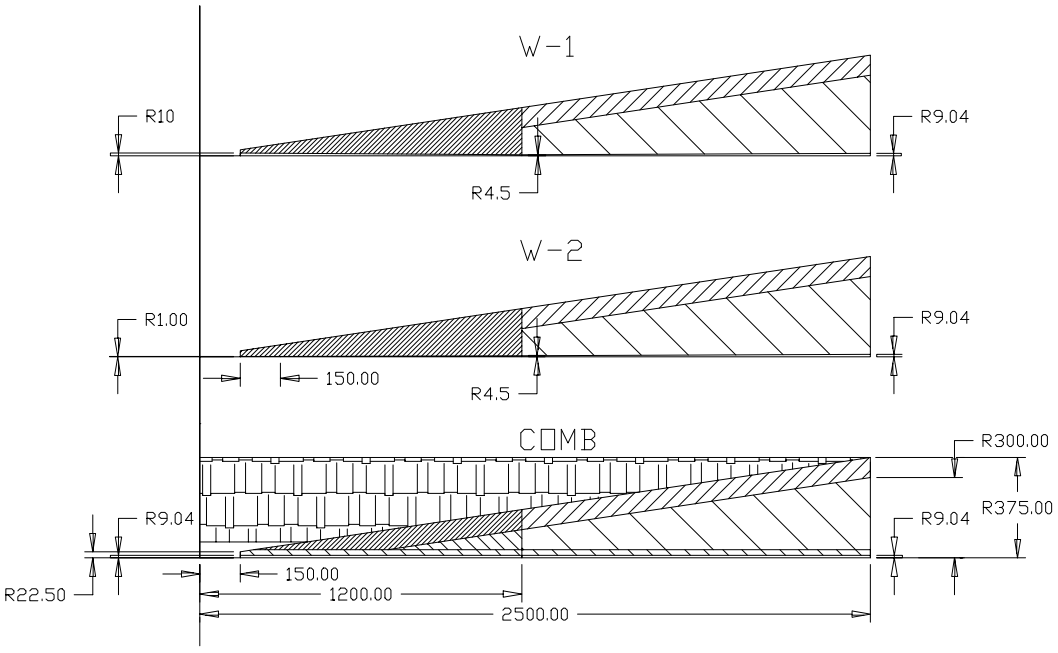

FIGURE 6. Configurations of collimating nozzles examined. Dimensions are in millimeters.

Table 2: e^+e^- fluence (cm^{-2} per crossing of 10^{12} muons per bunch) in the outward (L) and inward(R) parts of the inner (T1) and outer (T2) trackers and the central calorimeter (CH) for the cases with and without tungsten nozzle and with and without copper collimator in Configuration 1. For 2×10^{12} muons per bunch multiply by 2.

Nozzle	Collim	T1 (L)	T1 (R)	T2 (L)	T2 (R)	CH (L)
No	No	8.54×10^4	2.04×10^4	1.57×10^3	6.21×10^2	2.86×10^1
No	Yes	1.68×10^4	6.74×10^3	3.46×10^2	2.38×10^2	4.00×10^0
Yes	No	1.40×10^3	1.10×10^3	4.11×10^1	3.02×10^1	3.93×10^0
Yes	Yes	1.74×10^2	4.81×10^2	3.15×10^0	2.31×10^0	1.73×10^0
	$K_{max} =$	491	43	498	269	17

An additional way to suppress further the background levels can be a collimator between Q3 and B3 (see Fig. 1) with the smallest possible aperture. A copper collimator 50 cm long with 2.5σ radius aperture in these calculations provided up to a factor of 10 additional background reduction. The total maximum reduction K_{max} defined as a ratio of background levels in the given detector region without protective measures to that with a tungsten nozzle and copper collimator between Q3 and B3 magnets is given in the last row of the Table 2. It is as high as a factor of 500 at best, but for the larger radii in calorimeter it is "only" a factor of 20 to 40. Particle spectra in the detector are very soft in such a configuration: for all the regions considered background photons and electrons have energies below 100 MeV, being on the average just a few MeV. With a tungsten nozzle and copper collimator between Q3 and B3, the peak charged particle flux in the silicon tracker is of the order of 1000 cm^{-2} per crossing of two single bunches through the IR in opposite directions. The fluxes fall off very rapidly with radius.

Transverse distributions of e^+e^- flux in the central tracker are shown in Fig. 7 for Configurations 1 and 2. Backgrounds in the part of the tracker toward the ring center are significantly lower in Configuration 2 with a strong dipole field starting at 130 m from the IP [5]. On the outside the reduction is about a factor of 2 to 5. Fig. 8 shows the contribution to the energy deposition in the central tracker ($6 \leq r \leq 100$ cm) from muon decays along the IR in Configuration 2 [5]. Collimation and spoiling in the second focus region and in the long drift between the detector and the first dipole magnet can provide additional background reduction, but one needs to be very careful with beam halo handling in this case.

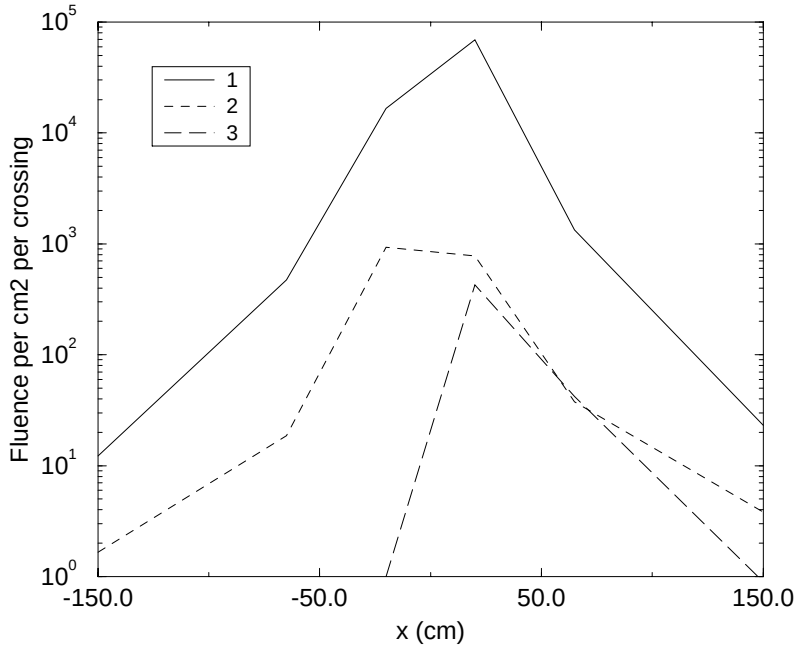

FIGURE 7. Distribution of e^+e^- flux in the central tracker horizontal plane. 1 - Configuration 1, no collimation, 2 - Configuration 2, with tungsten nozzle, 3 - Configuration 2, with tungsten nozzle.

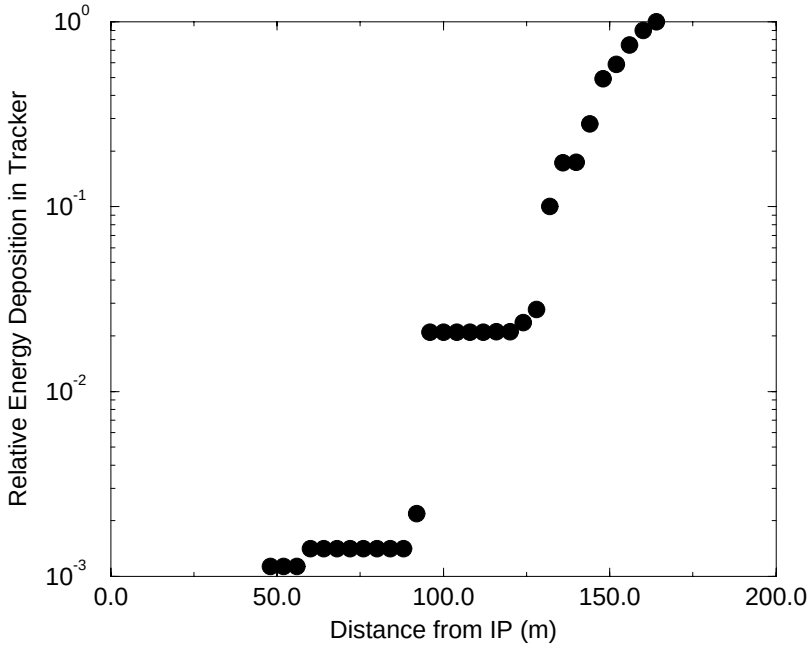

FIGURE 8. Cumulative energy deposition in the central tracker *vs* shower origin coordinate in Configuration 2.

Table 3: Particle fluence (cm^{-2} per crossing) in the central tracker (r =20 cm) and at the outer side of the endcap calorimeter (r =150 cm) due to 2 TeV muon decays (2×10^{12} muons per bunch) in Configuration 3.

Detector	n >0.00215 eV	γ >0.3 MeV	$e^{\pm}$ >0.3 MeV	$h^{\pm}$ >1 MeV	$\mu^{\pm}$ >1 MeV
Tracker	5×10^4	1.5×10^4	1000	80	3
Calorimeter	800	3×10^4	7000	0.3	0.2

The above results are confirmed for Configurations 3 and 4 with a much more realistic detector. In addition to e^+e^- and γ, hadrons and muons generated in the course of the electromagnetic shower development are taken into account. Fig. 9 shows a tagged decay distribution of energy deposited in the tracker as a function of the decay electron creation coordinate. Even with the optimal tungsten nozzle, the contribution from the $3 \leq L \leq 30$ m region to the background rates is very high. Particle fluxes in the central tracker and at the downstream end of the endcap calorimeter are presented in Table 3 for Configuration 3. In the endcap calorimeter the radial distributions are rather flat.

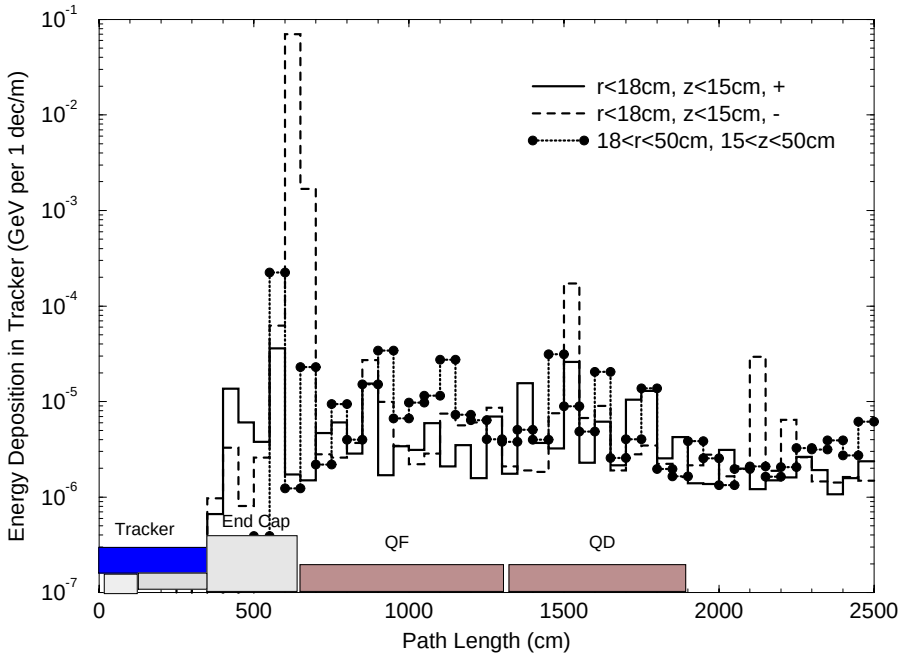

FIGURE 9. Tagged energy deposition in different regions of the central tracker due to $\mu \to e\nu\tilde{\nu}$ decays happened at given path length from the IP in Configuration 4.

Beam Halo

Beam halo backgrounds arise from muons which are lost some distance upstream of the detectors. These muons induce electromagnetic or hadronic showers either upstream or inside of the detector and can cause more serious problems. Beam particles injected with large momentum errors or betatron amplitudes will be lost within the first few turns. After this, an equilibrium level of losses will be attained as particles are promoted to larger betatron amplitudes via beam disruption from the collision point, beam-gas scattering, etc.

In simulations the beam is assumed to enter the IR with a non-truncated Gaussian profile. Muons outside $\pm 3\sigma$ will then interact and be scraped by the final arc magnets, low-beta quads, collimators, and detector components. The energy spectrum of muons averaged over the IR due to beam loss is presented in Fig. 10. The distribution of the muon interaction vertices in the vertical plane in the vicinity of the IP is rather symmetric, but in the horizontal plane there is a strong asymmetry related to the magnetic field. With an energy cut-off equal to 50 MeV for particles produced in muon interaction vertices, more than 95% of the vertices are direct e^+e^- pair production. Other processes, such as muon bremsstrahlung, deep inelastic nuclear interactions, muon decays and energetic knock-on electron production, are not so numerous, but secondary particles are more energetic (Fig. 11). Therefore the total energy going to these channels can be comparable to that of the pair production.

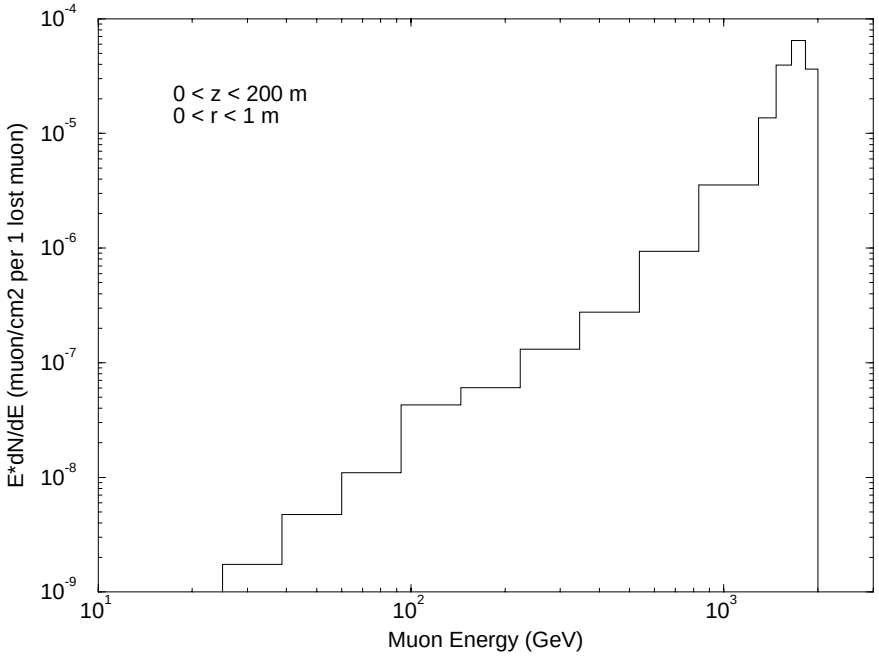

FIGURE 10. Muon energy spectrum due to 2 TeV muon beam loss at a limiting aperture at L = 200 m averaged over the IR region (Configuration 3).

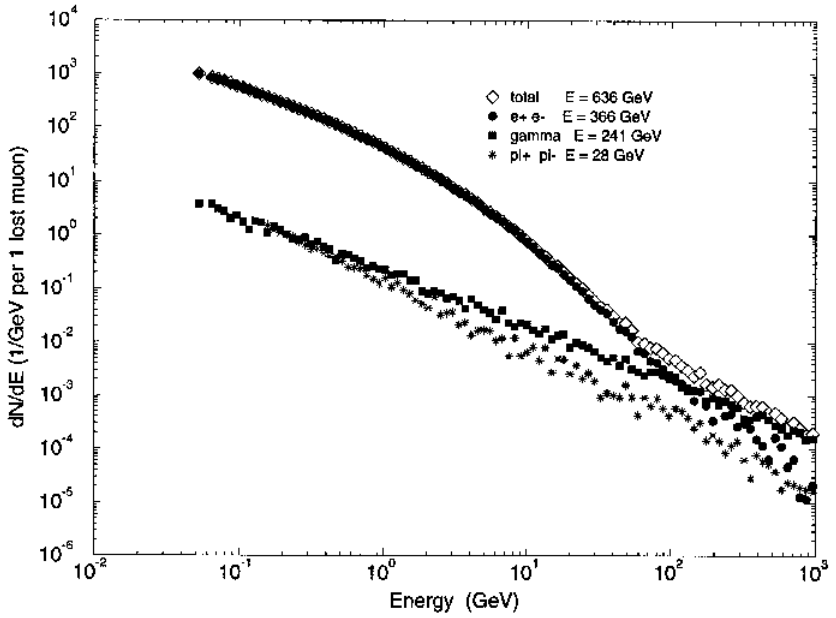

FIGURE 11. e^+e^-, γ and hadron energy spectra in muon interaction vertices for 2 TeV muon beam loss at a limiting aperture at L = 200 m (Configuration 3). Energies carried out by different particles are indicated.

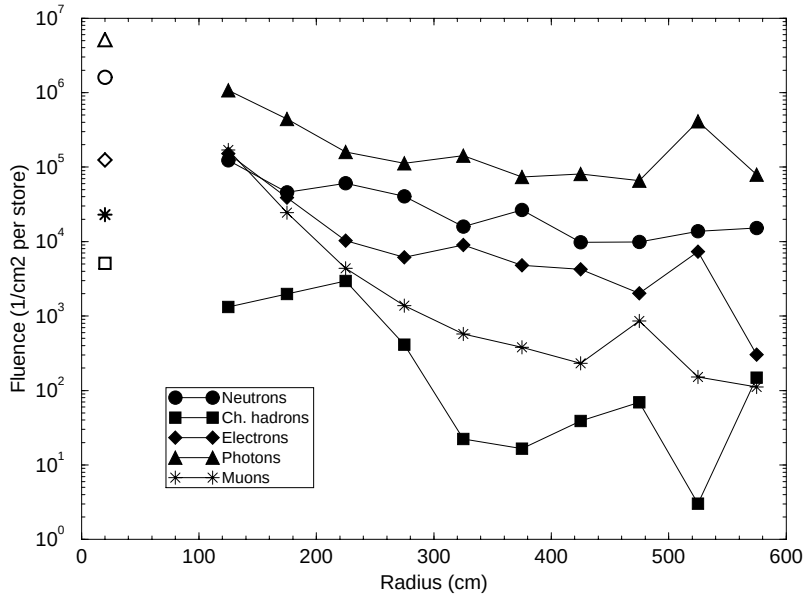

FIGURE 12. Particle fluences in the detector for 2 TeV beam halo loss (1% per store) at a limiting aperture at L = 200 m (Configuration 3): central tracker (open symbols) and radial distribution at the endcap calorimeter (filled symbols).

Particle fluences in the detector (Fig. 2) are shown in Fig. 12 for a 1% per store beam loss at a limiting aperture 200 m from the IP. One sees that all the components contribute to the background rates which for the few first turns (crossings) can significantly exceed those due to decays for the model considered. It is important that the protection strategy be different here. Collimators in the detector vicinity are drastically less effective. Beam scraping prior to injection to the storage ring and a dedicated beam cleaning system (with aperture smaller than any in the IR) a few kilometers from the IR are absolutely necessary elements of the collider to overcome the beam halo problem.

ENERGY DEPOSITION IN SC MAGNETS

Due to unavoidable $\mu \to e\,\nu\tilde{\nu}$ decays, about 300 to 900 W of power are deposited in every meter of the ring with a 10 to 30 Hz repetition rate. This results in a heat load to cryogenics which significantly exceeds the levels tolerated in existing SC magnets. This energy is deposited via electromagnetic showers induced in the beam pipe and in SC coils by high energy synchrotron photons and by decay electrons.

The calculations of energy deposition distributions in the storage ring components are performed for muon beam decays in Configurations 1 and 2. Even with a longitudinally uniform source, there is an increased rate at the β_{peak} location. With an 8 cm radius aperture, the photon flux at the 7.5 cm radius beam pipe and beam side of the SC coil is $\approx 10^9$ cm^{-2} and e^+e^- flux is $\approx 5\times 10^6$ cm^{-2} per store. There is a significant azimuthal dependence of energy deposition density due to the effect of the strong magnetic field. The peak energy deposition ≈ 3 mJ/g exceeds the quench limits for the magnet of the assumed type by almost an order of magnitude.

The way to mitigate the problem would be to intercept most of the shower energy, say at the nitrogen temperature level, inserting a liner between the beam pipe and the SC coils. A rather thin layer of a heavy material would do a good job both to reduce the peak energy deposition density (quench) and the total energy deposited at the liquid helium level (heat load to cryogenics). A 5-mm tungsten liner provides a factor of 8 reduction of the maximum energy deposition density. Fig. 13 shows the energy deposition azimuthal distribution with such a liner. Being azimuthally averaged, the effect is two times smaller. The lateral gradient of energy deposited in the SC coil is very strong both with and without a liner (Fig. 14).

A thicker liner has a bigger effect. Fig. 15 shows the azimuthally averaged energy deposition versus tungsten liner thickness in the 7.5 cm to 9.0 cm radial region in the first IR dipole. Even for the averaged deposition the reduction can be as high as a factor of 18 with a 10-mm liner and exceeding a factor of 30 reduction for the peak energy density. For the fixed inner radius (=7.5 cm) the effect of a thicker liner ($>$10 mm) is weaker. For a particular lattice, the liner thickness might be non-uniform: thicker in a horizontal plane (and in a vertical plane in the quadrupoles), consisting of rod-like insertions, and thinner in the rest of the aperture (see Fig. 13).

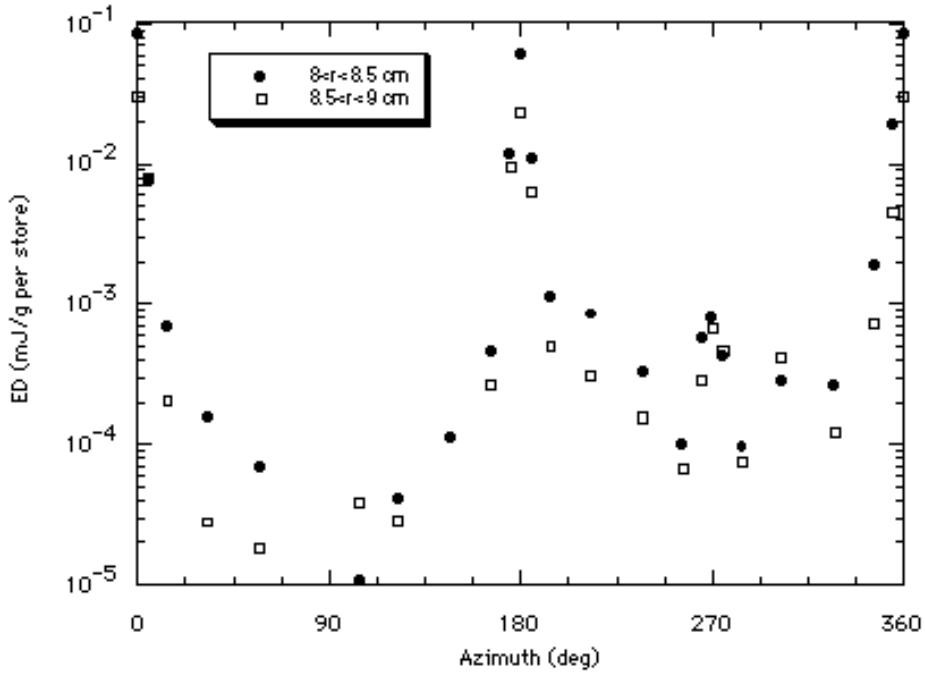

FIGURE 13. Azimuthal distribution of energy deposition density in the first SC cable shell of the first IR dipole with 5-mm tungsten liner.

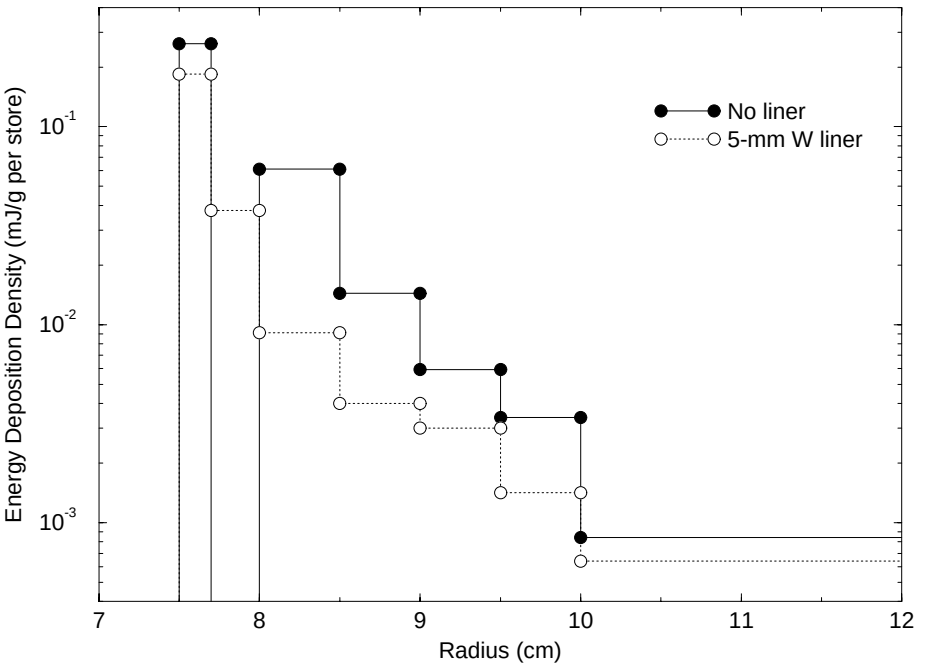

FIGURE 14. Azimuthally averaged radial distribution of energy deposition density in the first IR dipole with and without 5-mm tungsten liner.

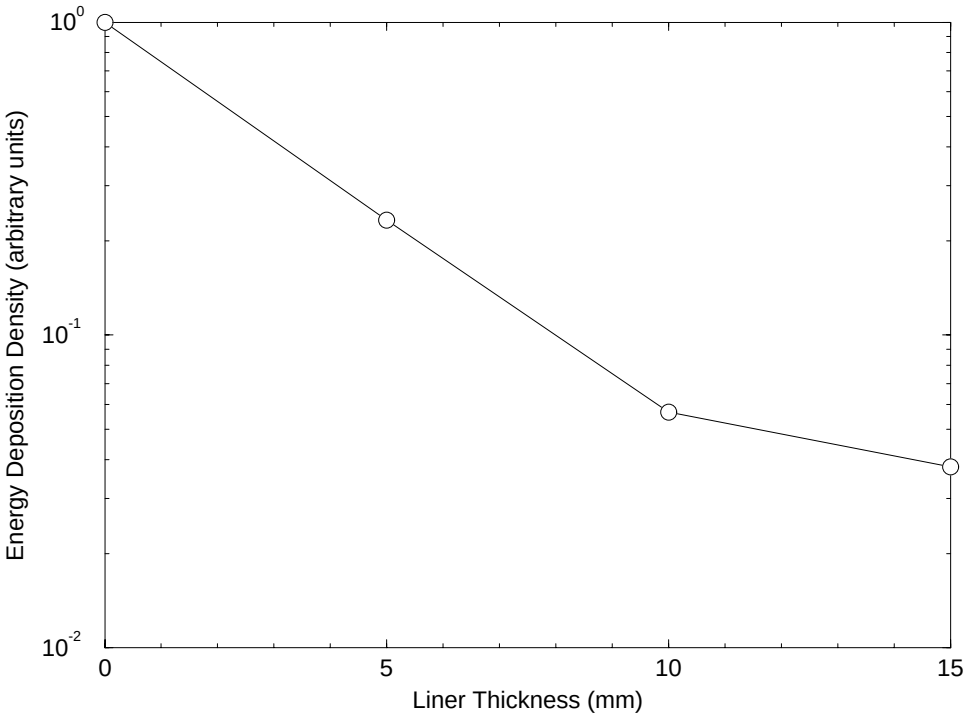

FIGURE 15. Attenuation of azimuthally averaged energy deposition density in the first SC cable shell as a function of the tungsten liner thickness.

CONCLUSIONS

A 2×2 TeV high-luminosity $\mu^+\mu^-$ collider offers exciting physics opportunities. The calculational tools developed allow reliable and detailed analyses of the background and radiation fields formed in machine and detector components. In the studies performed, the beam induced effects look severe, but can be mitigated with the proposed measures. There is a hope that with more work the design goals of this new generation project can be achieved.

ACKNOWLEDGMENTS

We thank K. Y. Ng, R. J. Noble, R. B. Palmer and A. V. Tollestrup for useful discussions.

References

[1] "Physics Potential and Development of $\mu^+\mu^-$ colliders", Sausalito–94, ed. by D. Cline, *AIP Conference Proceedings* **352** (1996).

[2] Palmer, R. B. et al., "Beam Dynamics Problems in a Muon Collider", in *ICFA Beam Dynamics Newsletter*, No. 8, pp. 27–33, August 1995; also BNL–61580 (1995).

[3] Palmer, R. B. et al., "High-Energy High-Luminosity $\mu^+\mu^-$ Collider Design", BNL–62041 (1995).

[4] Foster, G. W. and Mokhov, N. V., "Backgrounds and Detector Performance at a 2×2 TeV $\mu^+\mu^-$ Collider", in [1] pp. 178–190; also Fermilab–Conf–95/037 (1995).

[5] Gelfand, N. M. and Mokhov, N. V., "2×2 TeV $\mu^+\mu^-$ Collider: Lattice and Accelerator-Detector Interface Study", in *Proc. of 1995 Particle Accelerator Conference*, Dallas, May 1995; also Fermilab–Conf–95/100 (1995).

[6] Mokhov, N. V., "The Radiation Environment at Muon Colliders", in *Proc. of the 2nd Workshop on Simulating Accelerator Radiation Environments (SARE2)*, CERN, Geneva, October 1995.

[7] Polychronakos, V., presented at *2×2 TeV $\mu^+\mu^-$ Collider Collaboration Meeting*, Brookhaven, February 1995.

[8] Mokhov, N. V., "The MARS Code System User's Guide, Version 13(95)", Fermilab–FN–628 (1995).

[9] Striganov, S., *Nucl. Instruments and Methods* **A322**, 225-230 (1992); "Fast Precise Algorithm for Simulation of Ionization Energy Losses", *IHEP 92-80*, Protvino (1992).

[10] Kalinovskii, A. N., Mokhov, N. V., and Nikitin, Yu. P., *Passage of High-Energy Particles through Matter*, AIP, New York, 1989.

[11] Jackson, J. D., *Classical Electrodynamics*, 2nd Ed., J. Wiley, New York, 1975.

[12] "Review of Particle Properties", *Phys. Rev.* **D50**, No. 3 (1994).

[13] Bukin, A.D. and Grozina, N.A., *Comp. Phys. Communications* **78**, 287–290 (1994).

[14] Van Ginneken, A., "Fluctuations of Ionization Energy Loss and Simulation of Ionization Cooling", Fermilab–Pub–94/384 (1995).

[15] Vavilov, P. V., *JETP* **32**, 920 (1957).

[16] Kel'ner, S. R., *Yad. Fiz* **5**, 1092 (1967).

[17] Kabayakawa, K., *Nuovo Cimento* **B47**, 156–184 (1967).

[18] Van Ginneken, A., *Nucl. Instr. Meth.* **A251**, 21–39 (1986).

[19] Andreev, Yu. M., Bezrukov, L. B., and Bugaev, E. V., *Phys. of Atomic Nuclei* **57**, 2066–2074 (1994).

[20] Petrukhin, A. V. and Shestakov, V. V., *Canad. J. Phys.* **46**, 337 (1968).

[21] Bezrukov, L. B. and Bugaev, E. V., *Sov. J. Nucl. Phys* **33**, 635 (1981).

[22] Sakumoto, W. K. et al., *Phys. Rev.* **D45**, 3042–3050 (1992).

[23] Bloom, E. D. et al., SLAC–PUB–653 (1969); Armstrong, T. A. et.al., *Phys. Rev.* **D5**, 1640 (1972).

[24] Montanet, L. et al., *Phys. Rev.* **D50**, 1335 (1994).

[25] Armstrong, T. A. et al., *Nucl. Phys.* **B41**, 445 (1972).

[26] Caldwell, D. O. et al., *Phys. Rev.* **D7**, 1362 (1973).

[27] Bianchi, N. et al., *Phys. Lett.* **B325**, 333 (1994).

[28] Baishev, I. S., Kurochkin, I. A., and Mokhov, N. V., IHEP–91–118, Protvino (1991).

[29] Berman, B. L., and Fultz, S. C., *Rev. Mod. Phys.* **47**, 713 (1975).

[30] Mokhov, N. V., "Muons at LHC. Part 1: Beam Dumps", CERN/TIS–RP/TM/95–27 (1995).

[31] Van Ginneken, A., "MUSIM: Program to Simulate Production and Transport of Muons in Bulk Matter", Fermilab–FN–594 (1992). ERRATUM: Fermilab–FN–610 (1993).

[32] Tsai, Y., *Rev. Mod. Phys.* **46**, No. 4, 815–851 (1974).